REVIEW ARTICLE | FOCUS
https://doi.org/10.1038/s41566-019-0358-x
nature photonics

Photonic-chip-based frequency combs

Alexander L. Gaeta[1]*, Michal Lipson[2] and Tobias J. Kippenberg[3]

Recent developments in chip-based nonlinear photonics offer the tantalizing prospect of realizing many applications that can use optical frequency comb devices that have form factors smaller than 1 cm^3 and that require less than 1 W of power. A key feature that enables such technology is the tight confinement of light due to the high refractive index contrast between the core and the cladding. This simultaneously produces high optical nonlinearities and allows for dispersion engineering to realize and phase match parametric nonlinear processes with laser-pointer powers across large spectral bandwidths. In this Review, we summarize the developments, applications and underlying physics of optical frequency comb generation in photonic-chip waveguides via supercontinuum generation and in microresonators via Kerr-comb generation that enable comb technology from the near-ultraviolet to the mid-infrared regime.

Over the past decade, applications of optical frequency combs (OFCs) have rapidly grown across diverse areas of science and engineering, including chemical sensing, timekeeping, distance ranging, searching for exoplanets and as a source for wavelength-division multiplexing in photonic communications[1]. While most of these demonstrations were initially performed using tabletop systems, recent developments in chip-based nonlinear photonics offer the prospect of realizing comb devices in highly compact, portable, robust and fully integrated form factors that could make their use ubiquitous for a broad range of environments. For many applications in spectroscopy, and time and frequency metrology it is desirable that the comb bandwidth be extremely broad (for example, octave spanning for self-referencing via f–$2f$ interferometry[1]), which can only be achieved through nonlinear optical interactions that generate a broad range of new optical frequencies significantly beyond those in the initial laser field incident on the nonlinear medium. Two of the most remarkable examples that can produce such broad spectra are the processes of supercontinuum generation (SCG) in optical waveguides[2] and Kerr-comb generation (KCG) in microresonators[3].

In SCG[4], the pump field consists of a train of ultrashort pulses from a mode-locked laser, which is itself a frequency comb. The pulses are then passed through a waveguide and undergo a third-order (that is, $\chi^{(3)}$) nonlinear interaction in which the spectrum is extended via parametric four-wave mixing (FWM) processes (Fig. 1, left). For a sufficiently strong interaction and with suitable dispersion in the waveguide, the bandwidth of the comb can exceed an octave with a spacing that is determined by the pulse repetition rate of the mode-locked pump laser. In the process of KCG (Fig. 1, right), a passive microresonator is pumped near a cavity mode by a single-frequency, continuous-wave laser that produces gain via FWM at other cavity modes[5,6], and for sufficiently strong nonlinearity and with appropriate dispersion, a comb is generated with a spacing given by the free spectral range (FSR) of the microresonator. This process defied the notion that comb generation required a pulsed input and has been shown to allow for the generation of coherent OFCs[3] with a total spectral width that can also extend more than an octave.

Key underlying physics is shared by both SCG and KCG that results in fully coherent combs. Both rely on the formation of dissipative cavity solitons[7] for which nonlinearity is balanced by dispersion and gain compensates for loss, resulting in a stable pulse circulating within the cavity. In the case of SCG, a cavity soliton or solitary wave is formed within the mode-locked laser cavity that pumps the waveguide, and under suitable conditions can be described by the master equation[8], whereas in KCG the cavity soliton is formed in the microresonator and is described by the Lugiato–Lefever equation[9,10]. Both processes require careful control of the dispersion within the nonlinear medium to achieve phase matching of the parametric FWM processes that produces the extreme spectral broadening.

Chip-based platforms offer several key features for performing SCG and KCG compared with fibre-based platforms, which include high effective nonlinearities and the ability to perform strong dispersion engineering over a broad range of pump wavelengths that allows for phase matching of parametric processes over extremely broad bandwidths[11]. Table 1 shows a summary of the linear and nonlinear properties of various platforms that have been used to perform nonlinear photonics on a chip and whether KCG or SCG has been observed. Critical properties of these chip-based materials are the strong nonlinearity and the high refractive index contrast between the core waveguide and the cladding layer. For example, materials such as silicon and silicon nitride (Si_3N_4) have refractive indices of 3.4 and 2, respectively, at 1.55 μm and are typically covered by a silicon oxide cladding layer with an index of 1.46. This large index contrast allows for light with a wavelength λ to be strongly confined to an area smaller than λ^2, which further enhances the nonlinear interaction. More importantly, this tight confinement allows for dispersion engineering that offers control of the interaction to enhance and/or tailor the comb spectrum.

For some applications it may be desirable for the waveguide material to possess an intrinsic second-order nonlinearity $\chi^{(2)}$ that can be used to extend KCG to shorter wavelengths via second-harmonic and sum-frequency generation, for f–$2f$ interferometry, or to tune/modulate the microresonator resonance. The last column in Table 1 indicates whether the bulk material possesses intrinsic $\chi^{(2)}$. While bulk amorphous materials such as silica and silicon nitride do not possess an intrinsic $\chi^{(2)}$, in a waveguide geometry it is possible to induce an effective $\chi^{(2)}$ via the core/cladding interface[12], via stress[13] through material growth or via ion migration[14].

Figure 2a shows a plot of the refractive index of Si_3N_4 both as bulk and as a waveguide clad with silicon oxide, and Fig. 2b corresponds to the associated group-velocity dispersion (GVD). The origin of this dispersion engineering that results in the waveguide is due to the change in the effective index as the spatial extent of the waveguide mode increases from being tightly confined in

[1]Department of Applied Physics and Applied Mathematics, Columbia University, New York, NY, USA. [2]Department of Electrical Engineering, Columbia University, New York, NY, USA. [3]École Polytechnique Fédérale de Lausanne (EPFL), Institute of Physics, Lausanne, Switzerland.
*e-mail: a.gaeta@columbia.edu

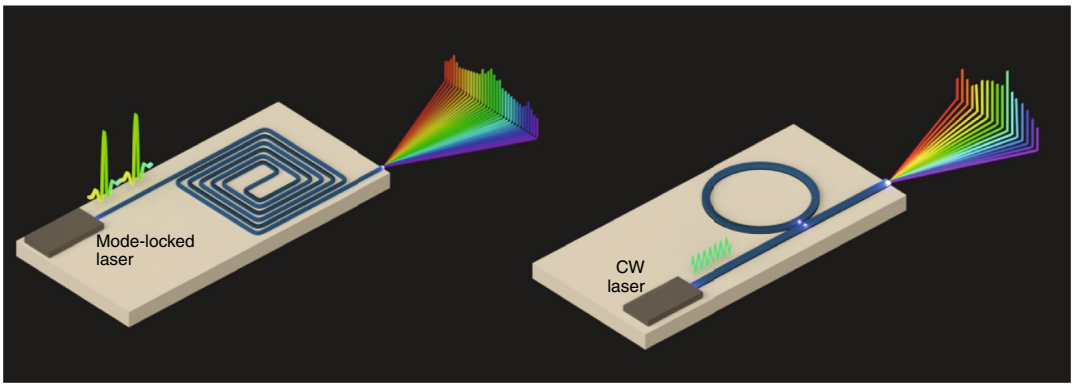

Fig. 1 | Chip-based frequency comb generation. Left: SCG via injection of a train of ultrashort pulses into a waveguide with a cross-section dispersion engineered to produce a broad optical frequency comb with a spacing determined by the inverse of the pulse repetition rate. Right: KCG via pumping with a single-frequency laser of a microresonator that is dispersion engineered to produce a broad spectrum with a comb spacing given by the FSR of the microresonator. CW, continuous wave.

Table 1 | Linear and nonlinear optical properties of various materials suitable for chip-based nonlinear photonics

Material	Refractive index	Nonlinear index ($m^2\ W^{-1}$)	Transparency (μm)	KCG observed	SCG observed	$\chi^{(2)}$
Silica	1.45	3×10^{-20}	0.2–4	Y	Y	N
Si	3.47	5×10^{-18}	1.2–8	Y	Y	N
α-Si-H	3.73	1.7×10^{-17}	0.78–4	N	Y	N
Si_3N_4	2.0	2.5×10^{-19}	0.4–4.6	Y	Y	N[c]
Hydex	1.7	1.15×10^{-19}	0.29–7	Y	Y	N
AlN	2.12	2.3×10^{-19}	0.2–13.6	Y	Y	Y
GaN	2.31	7.8×10^{-19}	0.36–13.6	N	N	Y
GaP	3.05	6×10^{-18}	0.54–10.5	Y	N	Y
Diamond	2.38	8×10^{-20}	0.22–>50	Y	Y	N
AlGaAs	3.3	2.6×10^{-17}	0.7–17	Y	Y	Y
SiGe[a]	3.59	2.7×10^{-18}	1.2–9.3	N	Y	N
Ge[b]	4.33	4.4×10^{-17}	1.8–15	N	N	N
$LiNbO_3$	2.21	1.8×10^{-19}	0.35–5	Y	Y	Y
As_2S_3	2.43	3.8×10^{-18}	0.6–11	N	Y	N
As_2Se_3	2.81	2.4×10^{-17}	1–14	N	Y	N

Columns 5 and 6 correspond to whether KCG and SCG, respectively, have been observed. Column 7 indicates whether the material possesses a second-order optical nonlinearity. Y, yes; N, no. All parameters are values at 1.55 μm except for [a]at 4 μm and [b]at 3.2 μm. [c]Although bulk silicon nitride does not have an intrinsic $\chi^{(2)}$, an effective $\chi^{(2)}$ response can be induced via stress or the photogalvanic effect.

the high-index core at short wavelengths to primarily residing in the low-index oxide at longer wavelengths; this can yield an effective GVD that offers little resemblance to the intrinsic GVD of the bulk material[11].

In addition to phase matching the parametric FWM gain process, this dispersion engineering enables expansion of the comb bandwidth through the controllable generation of dispersive waves (DWs), also known as Cerenkov radiation[15]. Dispersive waves are a result of a phase-matched process in the presence of dispersion that is of a higher order than the GVD that can result in the transfer of energy from the region near the pump wave to spectral components that can be as far as an octave away. The frequencies at which DWs are generated are determined by the dispersion function

$$D(\delta) = \sum_{n-2,3,\ldots} \frac{\beta_n}{n!}\delta^n \quad (1)$$

where δ is the frequency detuning from the frequency ω_0 of the pump wave and $\beta_n = \partial^n k/\partial\omega^n\,|_{\omega=\omega_0}$ is the nth-order dispersion parameter, and $k(\omega)=n(\omega)\omega/c$ and $n(\omega)$ are the propagation constant and effective refractive index, respectively, for the waveguide mode and include dispersion contributions that are both intrinsic to the material and from waveguide confinement. Since the nonlinear contribution to the index change is typically small, the location of the peaks of the DWs are nearly given by frequencies corresponding to the zeros of the dispersion function $D(\delta)$, which in the absence of dispersion higher than third-order dispersion consists of a single DW located at the frequency $\delta_{DW} \sim 3|\beta_2|/\beta_3$ from the pump. Example spectra produced via SCG (Fig. 2c) and KCG (Fig. 2d) with the Si_3N_4 waveguide cross-section in Fig. 2a,b both show signatures of DWs located at the corresponding zeros of D in Fig. 2b.

Comb generation based on supercontinuum generation

The demonstration[2] that pulses from a mode-locked oscillator could be spectrally broadened to beyond an octave of bandwidth using photonic crystal fibre represented a revolution in OFCs and led to the realization of self-referenced combs in which the frequency of the comb components could be determined to extremely high precision (<10^{-15}) (ref. [1]). While the resulting nonlinear pulse

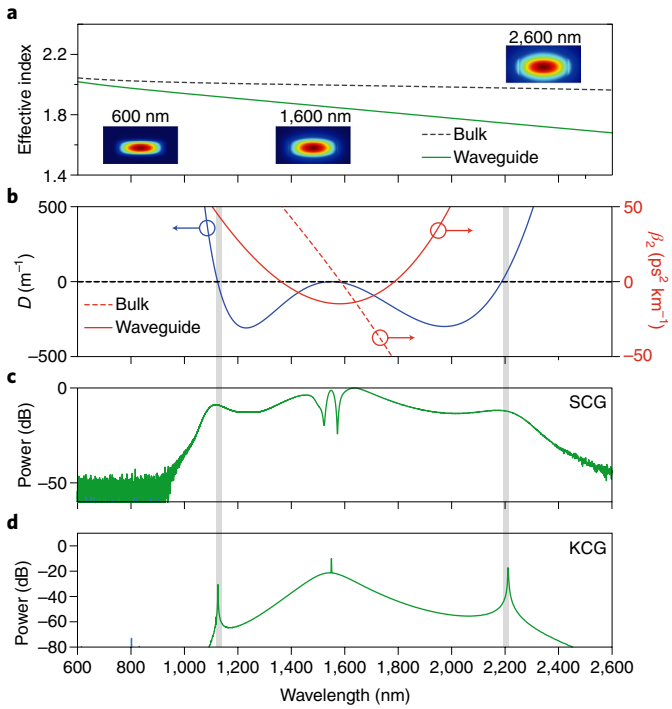

Fig. 2 | Dispersion engineering for comb generation. a, Effective index for bulk Si_3N_4 (dashed line) and that predicted for a 730 × 2,580 nm Si_3N_4 waveguide with oxide cladding (solid green). The images show the theoretically predicted intensity distributions for the fundamental mode at different wavelengths. **b**, Corresponding GVD of bulk Si_3N_4 (dashed red) and waveguide (solid red) and dispersion function D (solid blue). **c**,**d**, Spectra produced via SCG in the 5-cm-long waveguide (**c**) and via KCG in a microresonator (**d**), both with waveguide cross-sections as in **a**. The vertical grey lines show zeros of D that are in close agreement with the DWs generated in both spectra.

propagation dynamics that produces such broadening is complex and depends on numerous factors, the key aspect is that dispersion engineering allows for the pulses to undergo significant self-phase modulation before undergoing dispersive broadening and enhancing various FWM processes and DW generation. The spatiotemporal nonlinear dynamics for the amplitude $A(z, t)$ of the field inside the waveguide is well modelled by the 1D nonlinear envelope equation[16]

$$\frac{\partial A}{\partial z} = \left[i \sum_{m\geq 2} \frac{\beta_m}{m!} \left(i\frac{\partial}{\partial \tau} \right)^m + i\gamma \left(1 + \frac{i\partial}{\omega_0 \partial \tau} \right) \left(\int_{-\infty}^{\infty} R(\tau') |A(z, \tau - \tau')|^2 \, \mathrm{d}\tau' \right) \right] A \quad (2)$$

where z is the propagation distance inside the waveguide, $\tau = t - z/v_g$ is the retarded time for the pulse travelling at the group velocity v_g, $\gamma = \omega_0 n_2 / A_{\mathrm{eff}} c$ is the nonlinear parameter, n_2 is the nonlinear index coefficient, A_{eff} is the effective area of the waveguide and $R(\tau)$ is the Raman response function. This equation enables modelling of the supercontinuum process for spectral bandwidths up to an octave. Extensive modelling of SCG in photonic crystal fibres has led to a relatively complete understanding of the resulting features and shapes of the resulting spectra and the coherence properties[4]. The resulting spectra depend sensitively on the characteristics of the input pulse, the dispersive, electronic and nuclear contributions to the nonlinear refractive index, and effects such as self-phase modulation, self-steepening, soliton compression and fission, DW generation and stimulated Raman scattering typically all occur, and their interplay results in complex dynamics that can be well described by the nonlinear envelope equation[4,17].

A key property of the generated comb for many applications is the optical coherence across the generated spectrum. The coherence can be quantified by calculating the first-order degree of coherence

$$g_{12}^{(1)}(\omega) = \frac{\langle A_i(\omega) A_j(\omega) \rangle}{\sqrt{\langle |A_i(\omega)|^2 \rangle \langle |A_j(\omega)|^2 \rangle}} \quad (3)$$

where the angle brackets denote an ensemble average for independently generated pairs ($i \neq j$) of spectra $A_i(\omega)$ (ref. [4]). The function varies between 0 and 1 for fully incoherent and coherent spectra, respectively. High coherence is essential, for example, to stabilize the comb through f–$2f$ interferometry[1] in which the frequency-doubled red components of the spectrum interfere with the blue part of the spectrum separated by an octave or to perform dual-comb spectroscopy (DCS) that requires heterodyning of two separately generated frequency combs[18]. Most of the early experiments investigating spectral broadening and SCG in chip-based waveguides focused on generating broad spectra without determining the resulting coherence. Typically, to produce coherent spectra it is necessary to operate in the regime in which coherence of the initial mode-locked ultrashort pulse train is preserved and self-phase modulation is the dominant mechanism that produces the initial broadening rather than through the growth of spectral components from noise via parametric FWM gain (that is, modulational instability)[4]. As such, it has been desirable to operate with pulses that are relatively short (that is, <100 fs) with soliton numbers $N < 10$ or in the slightly normal-GVD regime, the latter of which requires higher pulse energies than in the anomalous-GVD regime. Dispersive wave generation, which can be fully coherent, can be tuned via dispersion engineering and can be applied to enhance either the long- or short-wavelength side (Fig. 3), and is essential, for example, for f–$2f$ interferometry to stabilize the comb.

Material platforms for SCG. *Silicon.* Initial experiments[19] in Si (that is, crystalline) waveguides observed frequency broadening of ultrashort pulses at 1.3 μm. By using ultrashort pulses at wavelengths beyond 2.1 μm to minimize two-photon and free-carrier absorption effects[20], broader spectra and DW generation could be achieved[21], including octave-spanning spectra[22]. A key demonstration[23] showed that by pumping an air-clad Si nanowaveguide with 2,290-nm pulses with only 16 pJ of energy, a coherent octave-spanning supercontinuum spectra could be generated that produced coherent beat notes in an f–$2f$ interferometer. More recently, experiments have focused on extending SCG further into the mid-infrared. For example, using silicon-on-sapphire waveguides, SCG from 1.9–6 μm was observed using 3.7-μm pumping[24] and spectra from 2–5 μm were achieved in an air-clad geometry[25]. Hydrogenated amorphous Si (a-Si-H) is a particularly attractive nonlinear material for nonlinear photonics due to its large nonlinear refractive index and ease of fabrication for photonic devices, although at the expense of higher linear and nonlinear losses. Early experiments in a-Si-H waveguides observed large spectral broadening of an octave[26,27], and ensuing experiments pumping at 1,550 nm (ref. [28]) showed good coherence[29] for 180-fs input pulses, and also observed degradation in the performance in terms of loss and nonlinearity as higher powers were injected into the waveguide for picosecond pulses but not for femtosecond pulses[28].

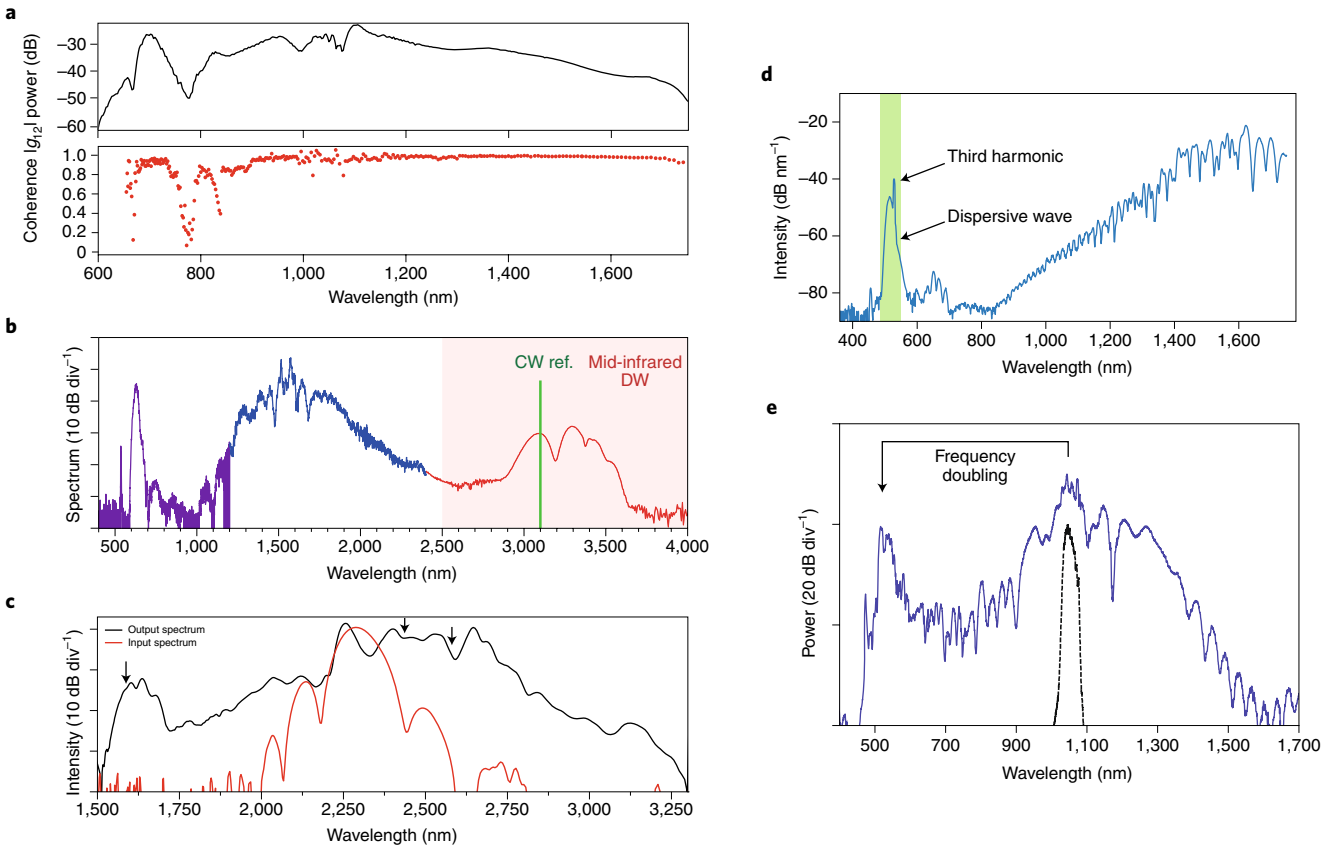

Fig. 3 | Coherent comb SCG spectra generated in chip-based platforms with DW generation via dispersion engineering. a, Top: SCG in Si_3N_4 waveguide. Bottom: measured coherence illustrating that the strong DW near 700 nm is fully coherent[35]. **b**, DW generation in Si_3N_4 a full octave away towards the mid-infrared from the pump field at 1,550 nm (ref. [39]). **c**, The input (red) and output (black) spectra generated in a Si nanowaveguide. The arrows indicate the wavelength position where the phase coherence measurements were performed[23]. **d**, DWs generated in Si_3N_4 near the third-harmonic that allows for efficient f–3f self-referencing[41]. **e**, DW generation (blue) in silica rib waveguides an octave from the initial pump wave (black dashed)[58]. Figure adapted from: **a**, ref. [35], OSA; **b**, ref. [39], Springer Nature Limited; **c**, ref. [23], under a Creative Commons licence (https://creativecommons.org/licenses/by/4.0/); **d**, ref. [41], OSA; **e**, ref. [58], under a Creative Commons licence (https://creativecommons.org/licenses/by/4.0/).

Silicon nitride. The first studies[30] investigating SCG in silicon nitride waveguides with 1.3 μm pulses illustrated a number of its features as an excellent nonlinear platform for SCG, including large effective nonlinearity and low linear and nonlinear losses, and the ability to generate spectra that could be far broader than an octave with the potential for generating light from the visible to the mid-infrared using near-infrared or telecom sources. Further experiments showed even broader spectra with bandwidths as high as 495 THz (ref. [31]) and deep into the visible regime with pumping at 795 nm (ref. [32]). Silicon-rich nitride waveguides have also shown promise for SCG[33] with high nonlinearity, and coherent octave-spanning combs have been generated[34]. Spectral interferometric measurements[35] confirmed theoretical simulations that spectra generated in Si_3N_4 were highly coherent across these bandwidths, which was also supported in experiments that demonstrated f–2f interferometry, carrier–envelope offset detection[36] and stabilization[37]. Through appropriate dispersion engineering, coherent DWs can be generated either to shorter wavelengths[38] or into the mid-infrared[39] from the pump. Further work has shown that octave-spanning OFCs based on Si_3N_4 can be used to perform optical clock comparisons with a calcium atomic clock laser at 657 nm and a 1,550-nm cavity-stabilized laser[40]. Observation of simultaneous third-harmonic generation and SCG[41] allows for self-referencing via f–3f in a single waveguide (Fig. 3d). Although bulk Si_3N_4 is amorphous, second-harmonic generation may also be simultaneously observed with SCG in waveguides due to an effective $\chi^{(2)}$ created via stress during the thin-film growth process[13,42] or due to electromigration[43], which via f–2f would also allow for self-referencing of the resulting comb without the need for an additional doubling crystal.

Chalcogenides. Owing to their relatively high refractive index and high nonlinear index chalcogenide glasses offer the ability to engineer the dispersion for telecom[44] and mid-infrared operation[45–47] with very high values of the nonlinear parameter γ. The first experiment demonstrating octave-spanning SCG on a chip utilized dispersion-engineered, ridge As_2S_3 waveguides clad with a polymer glass and 610-fs input pulses[48]. While various demonstrations of octave-spanning spectra have been made with 1,550-nm pump pulses[49], particularly exceptional performance has been exhibited in the mid-infrared[47]. While coherent frequency combs have been predicted for chip-based systems[49], to date, no coherent OFC has been experimentally confirmed using chalcogenide chip-based waveguides.

Other materials. A number of other materials, which include titanium dioxide[50] and InGaP (ref. [51]), have shown to be promising for SCG within a chip-based platform. Impressive on-chip SCG performance in the mid-infrared regime has also been shown with SiGe (refs. [52,53]) and germanium[54]. Materials such as aluminium nitride[55] and lithium niobate[56] are promising for SCG since they possess $\chi^{(2)}$ nonlinearities that allow for f–2f interferometry within the same waveguide. In silica ridge waveguides[57,58], DWs were generated

down to the ultraviolet, which could prove useful for spectroscopic applications in this regime.

Applications. While numerous applications in spectroscopy[59], and time and frequency metrology have already been demonstrated with combs produced via SCG using microstructured fibres or highly nonlinear fibres, with commercial systems now available, fewer demonstrations of such applications have used chip-based SCG to date since these applications are implemented using a fibre setting. We expect that as mode-locked lasers are further miniaturized and eventually integrated on a photonic chip that applications with on-chip SCG devices will rapidly multiply.

Spectroscopy. A chalcogenide-based SCG system was exploited to perform optical absorption measurements of microfluidic solutions[60].

Telecommunications. For communications based on wavelength-division multiplexing, OFCs based on SCG offer the prospect of producing many single-frequency sources that will all be highly stabilized to a frequency grid via stabilization of the mode-locked pump laser. By performing SCG in an AlGaAsOI-chip waveguide, up to 661 Tb s^{-1} data rates could be supported using a single-mode, 30-core fibre[61].

Microresonator-based comb generation

Generation of OFCs[3] and soliton mode-locking in microresonators are based on pumping a microresonator with a single-frequency pump field, and through appropriate tuning of the frequency and/or the amplitude of the pump field it is possible to excite dissipative Kerr solitons (DKSs)[62], which has unlocked the full potential for creating broadband, fully coherent combs. Since the early work on KCG[63], researchers have shown that the system can show rich and complex nonlinear behaviour[64], including bistability, chaos, single- and multiple-soliton formation, soliton crystals[65] and breather instabilities[66–68].

The dynamics of comb generation in microresonators is well described by the Lugiato–Lefever equation[69–71] in which higher-order GVD terms and stimulated Raman scattering are included[72,73]

$$T_R\frac{\partial A}{\partial t} = \sqrt{\kappa}A_p + \left[-\frac{\alpha}{2}-\frac{\kappa}{2}-i\delta_0 + iL\sum_{m\geq 2}\frac{\beta_m}{m!}\left(i\frac{\partial}{\partial\tau}\right)^m + i\gamma L\left(\int_{-\infty}^{\infty}R(\tau')|\,A(z,\tau-\tau')\,|^2\,\mathrm{d}\tau'\right)\right]A \quad (4)$$

where A is the intracavity field, A_p is the amplitude of the incident pump field in the bus waveguide just before the coupling region to the microresonator, T_R is the microresonator round-trip time, t is the 'slow' (compared with T_R) time variable, and τ is the 'fast' time that corresponds to the local time within the cavity, L is the cavity length, δ_0 is the detuning of the cavity resonance from the pump frequency, α is the round-trip loss, κ is the coupling coefficient between the bus waveguide and the microresonator, and $R(\tau)$ is the Raman response function. An example of the predicted dynamical behaviour as the frequency of the pump laser is passed through the cavity resonance of a silicon microresonator to excite the single-soliton mode-locked state is shown in Fig. 4 (ref. [74]). As the pump detuning varies, the system evolves from the generation of mini-combs[75], to a chaotic (that is, high-noise state) regime, and eventually into multiple- and single-cavity-soliton states. Higher-order dispersion that governs the formation of DWs also facilitates in reaching the soliton-mode-locked state[76].

The bandwidth of the mode-locked comb can be estimated by the soliton condition within the microresonator, which represents a balance between the nonlinear length $L_{nl} = 1/\gamma\,|A_0|^2$ and the dispersion length $L_{ds} = \tau_p^2/|\beta_2|$, where A_0 is the peak amplitude and τ_p is the pulse duration of the soliton. For the case of critical coupling (that is, $\alpha = \kappa$), the 3-dB comb bandwidth can be estimated to be[62,77]

$$\Delta\omega_{comb} \sim 0.63\sqrt{\frac{2\pi P_{in}\mathcal{F}_c}{\beta_2}} \quad (5)$$

where $\mathcal{F}_c = \pi/\alpha$ is the cavity finesse and P_{in} is the power of the pump field in the bus waveguide just before the coupling region to the microresonator. Thus, to produce the broadest soliton-mode-locked combs, it is desirable to operate in the slightly anomalous-GVD regime (that is, small β_2). However, higher-order dispersion can significantly determine the resulting shape and bandwidth of the comb[78,79]. As discussed above, DWs can significantly extend the generated spectrum and produce significant enhancements near the peaks that can be useful for f–$2f$ interferometry and stabilization of the comb spectrum.

The first experimental observation of KCG was in silica microtoroids[3] and the equidistant nature of the comb was demonstrated by comparing it to a mode-locked femtosecond laser comb. Soon after, KCG was also observed in crystalline CaF_2 whispering-gallery-mode microresonators[80,81]. Since such systems rely on tapered fibres for coupling, making such systems robust and immune to environmental perturbations is challenging due to the nature of the evanescent coupling of the nanotapered fibre and the microresonator. Kerr combs in a monolithic chip-based platform were soon after observed in Si_3N_4 (ref. [82]) and Hydex glass[83]. Since then, KCG has been demonstrated in many different chip-based platforms and exhibits universal behaviour. In the early stages of development, a complete understanding of the complex and rich dynamical behaviour of this system had not been formulated and in nearly all cases the observed combs were not coherent and thus were characterized by high noise and lacked the high-precision comb spacing that is desirable for many applications. Nevertheless, there are conditions for which it is possible to observe low-noise combs without exciting the soliton-mode-locked states. For example, for the case in which the parametric gain condition favours excitation of the closest pair of modes one FSR from the pump mode, the resulting comb is known as a 'natively spaced comb'[75] and creates what are known as Turing rolls, which exhibit low noise but typically have bandwidths that are relatively narrow.

Evidence of soliton-mode-locked combs was observed in terms of low radio-frequency (RF) noise, pulsed output[84] and high-precision comb spacing[85], and a comprehensive understanding of the cavity soliton and multi-soliton formation processes was established by Herr et al.[62] in MgF_2 and then in Si_3N_4 structures[86]. Since then DKSs have been observed in a number of platforms[10], and the key signatures of cavity soliton formation include: (1) the observation of steps in the transmitted power of the pump wave in the bus waveguide as it is tuned through the cavity resonance, which is undergoing shifts both to thermal effects and the nonlinear refractive index such that solitons are generated on the 'red' side of the cavity resonance; (2) the spectral shape of the central region of the comb spectrum has the functional form of a sech for a single soliton, consistent with that of the predicted cavity soliton; (3) the output consists of ultrashort pulses with a period of the round-trip time or a subharmonic thereof; and (4) low RF noise. Figure 5a shows an example of the soliton steps observed as the field is tuned into resonance, leading to steps in the transmission that represent different soliton states[87]. A more detailed evolution is shown in Fig. 5b that goes through various regimes including modulation instability, chaos, and multiple- and single-soliton states[88]. It is important to note that the generated output frequency comb consists of a strong continuous-wave component at the pump frequency with a relatively weak underlying comb. For the case of excitation of the

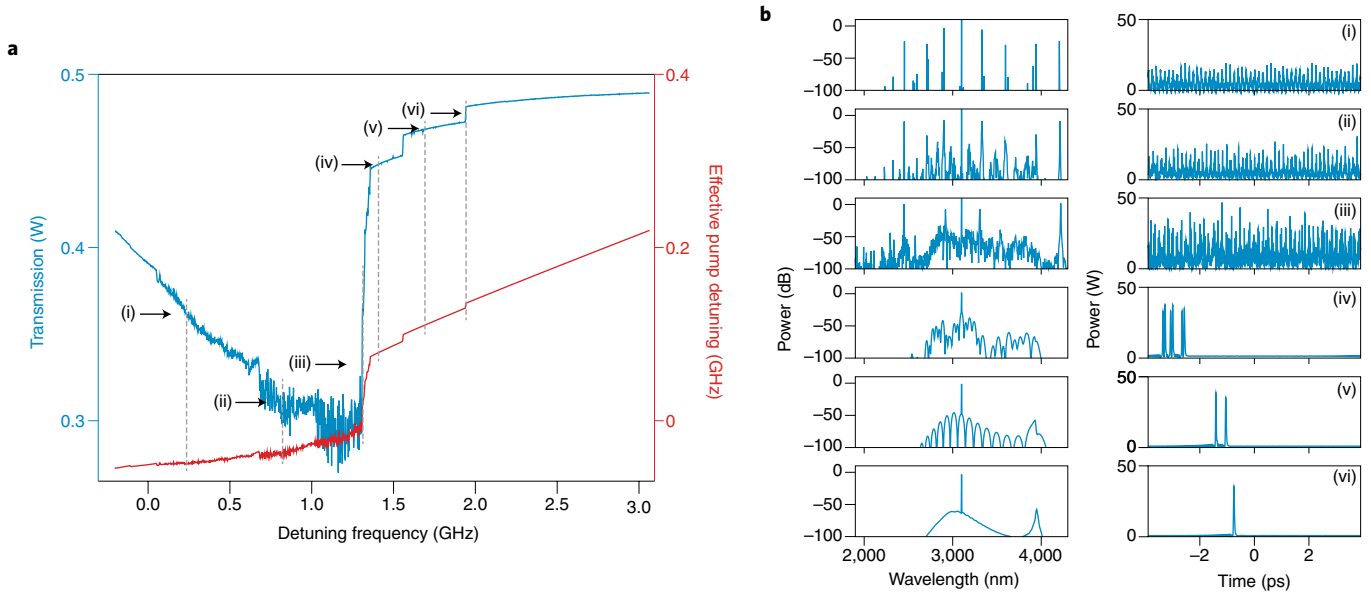

Fig. 4 | Numerical simulation of soliton formation in a silicon microresonator. a, Transmission and effective pump–cavity detuning when scanning a pump laser over a cavity resonance. The effective pump–cavity detuning subtracts the resonance shift due to the Kerr effect and free-carrier dispersion from absolute pump detuning. A series of abrupt transmission steps occur in the effective red-detuning regime. **b**, Optical spectra (left) and intracavity temporal behaviour (right) at different positions (i–vi) in the scan. The plots associated with (i–iii) are in the effective blue-detuning regime, while plots (iv–vi) are in the effective red-detuning regime. The transition to mode locking and soliton formation occurs between (iii) and (iv), as the pump frequency is tuned across the zero effective pump detuning point. As the laser is tuned, primary sidebands are generated through modulation instability and cascaded FWM (i), mini-combs are generated around each primary sideband (ii), with further intracavity power building up, different sets of mini-combs overlap, producing high-noise temporal behaviour (iii), a multiple (six)-soliton state occurs with a complex, structured optical spectrum (iv), a two-soliton state is produced (v), and the single-soliton state with a smooth optical spectrum is reached (vi). States with different numbers of solitons correspond to the transmission steps shown in **a**. Figure adapted from ref. [74], OSA.

single-soliton state, the ratio of the power in the comb to the input pump power is typically 1–3%. This efficiency can be increased roughly linearly with the number of cavity solitons that are excited within the microresonator.

In addition to tuning the pump frequency, a number of approaches have been developed to reach the soliton-mode-locked state, such as rapidly varying the microresonator resonance thermally[89], the pump power[90] or the pump phase[91]. Figure 5c shows an example of the resulting spectra achieved via different rapid thermal tuning of the microresonator to achieve $N = 1$, 2 and 4 soliton states[89]. These techniques may prove to be particularly important for implementation in real-world systems, since it can be challenging to tune the pump laser by tens of gigahertz or there may be applications in which it is desirable to use the same pump field to soliton-mode-lock two separate microresonators such as for DCS[92] or for synchronization of different microresonator combs[93].

KCG can also occur in the normal-GVD regime. Under suitable conditions, dark[94,95] or bright pulses[96] can be excited with low noise, which can be interpreted as the interlocked switching waves where the falling edge of one wave associated with one bistable state and the rising edge of the second wave corresponding to the other state combine to produce a pulse[97]. Generation of such localized pulses, termed a 'platicon'[98], can be assisted by mode coupling[96] that gives rise to an intracavity modulational instability[99] such that the strength of the coupling determines the bandwidth of the comb. Such normal-GVD combs offer a number of advantages over soliton-mode-locked combs including higher conversion efficiency from the pump to the comb and flatter comb spectra, which could be important for applications such as telecommunications[98].

Mode coupling can play a critical role in the KCG process[100]. This coupling can occur from frequency degeneracy of different spatial modes[100], polarization modes[101] or dual-cavity modes[96]. The resulting avoided crossings leads to a localized disturbance in the dispersion, which can be inferred as a relatively narrow dispersive shape in the comb spectrum that can be well modelled and can disrupt the formation of cavity solitons[100]. However, as mentioned above, mode coupling can facilitate the generation of combs in the normal-GVD regime[96].

The generation of Kerr combs and the dissipative soliton formation process can be strongly influenced by the presence of Raman scattering[102,103], which may set fundamental limits on the bandwidth and comb spacing. For the case in which the Raman linewidth is broad in comparison to the soliton bandwidth and extends down to the pump field, the Raman effect is predicted to lead to red-shifted solitons[104,105] in which the peak of the soliton spectrum is shifted to a wavelength longer than that of the pump frequency. Further theoretical analysis[106] has shown that the Raman effect in this regime can limit the comb bandwidth and the lower limit of the soliton duration. More complex behaviour can result in a 'trapped' Stokes soliton that coexists with the fundamental DKS by travelling in a higher-order mode as observed in a the silica wedge microresonator[107]. In the opposite limit in which the Raman linewidth is narrow compared with the comb spacing, Raman oscillation (that is, lasing) can compete with and disrupt comb formation[108] and cavity-soliton formation. This can be overcome by suppressing the Raman gain by operating with a sufficiently large FSR such that the Raman gain peak is located between two microresonator modes, which results in the following condition on the FSR to achieve Kerr-comb formation and mode-locking[108]:

$$\mathrm{FSR} > \frac{\Gamma_\mathrm{R}}{2\pi}\left(\frac{g_\mathrm{R}}{g_\mathrm{K}} - 1\right)^{1/2} \quad (6)$$

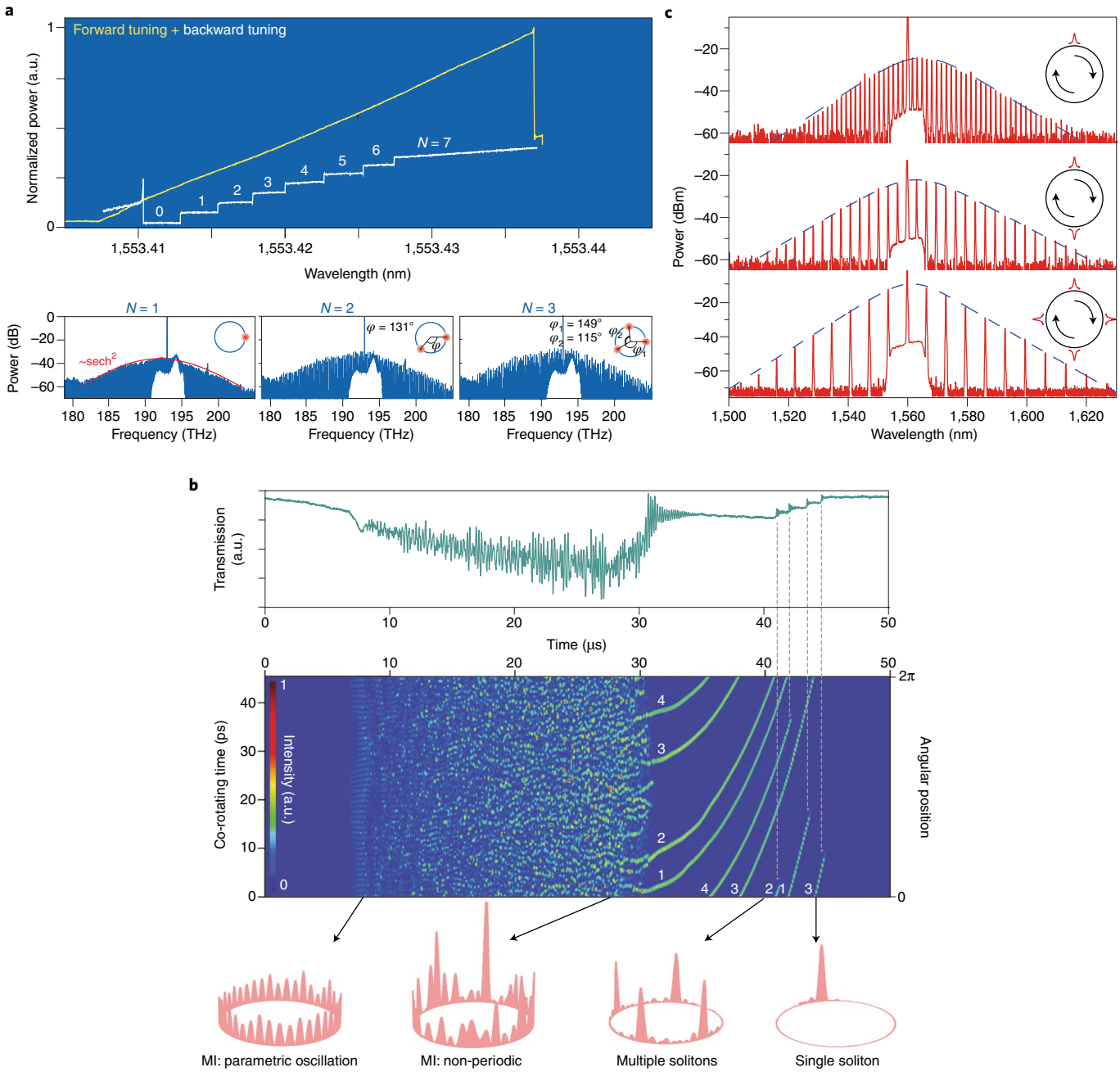

Fig. 5 | Experimental observation of soliton steps and generation of multiple soliton states. a, Top: experimental trace in the forward tuning of the laser into resonance of a SiN microresonator (yellow curve) followed by one trace in the backward tuning (white curve) with successive switching of multiple-soliton states from $N = 7$ to $N = 0$ (no solitons). Bottom: frequency comb spectra in soliton states with $N = 1$, 2, 3, measured during the backward tuning[87]. **b**, Top: pump power transmission of a silica microresonator as the pump frequency is tuned from higher to lower frequency, exhibiting multiple steps indicative of soliton formation. Middle: imaging of soliton formation corresponding to the scan where the *x* axis is time and the *y* axis is time in a frame that rotates with the solitons (full scale is one round-trip time). The right vertical axis is scaled in radians around the microcavity. Four soliton trajectories are labelled and fold back into the cavity coordinate system. Bottom: soliton intensity patterns measured at four moments in time are projected onto the microcavity coordinate frame. The patterns correspond to initial parametric oscillation in the modulation instability (MI) regime, non-periodic behaviour, four-soliton and single-soliton states[88]. **c**, Thermal tuning of a Si_3N_4 microresonator[89] to achieve the $N = 1$, 2, 4 (top to bottom) soliton states in which the solitons are equally spaced within the microresonator leading to comb spacings of 1, 2 and 4 FSRs. Figure adapted from: **a**, ref. [87], Springer Nature Limited; **b**, ref. [88], under a Creative Commons licence (https://creativecommons.org/licenses/by/4.0/); **c**, ref. [89], OSA.

where g_R and $g_K = 2\gamma$ are the Raman and Kerr gain coefficients, respectively. If $g_K \geq g_R$, then pure KCG is always possible for any FSR, as is the case for CaF_2, for example, for which $g_K / g_R \sim 1$. However, in the opposite limit, Raman oscillation will dominate unless the FSR can be made sufficiently large. For example, in diamond at 1,560 nm, $g_R = 6$ cm GW^{-1} and $g_K = 0.2$ cm GW^{-1}, which indicates that soliton-mode-locked combs are only possible with an FSR > 454 GHz and is consistent with experimental observations[108]. Since for many crystalline materials, the Raman linewidth $\Gamma_R/2\pi$ is relatively narrow, where Γ_R is the round-trip time, and the gain is large, the Raman

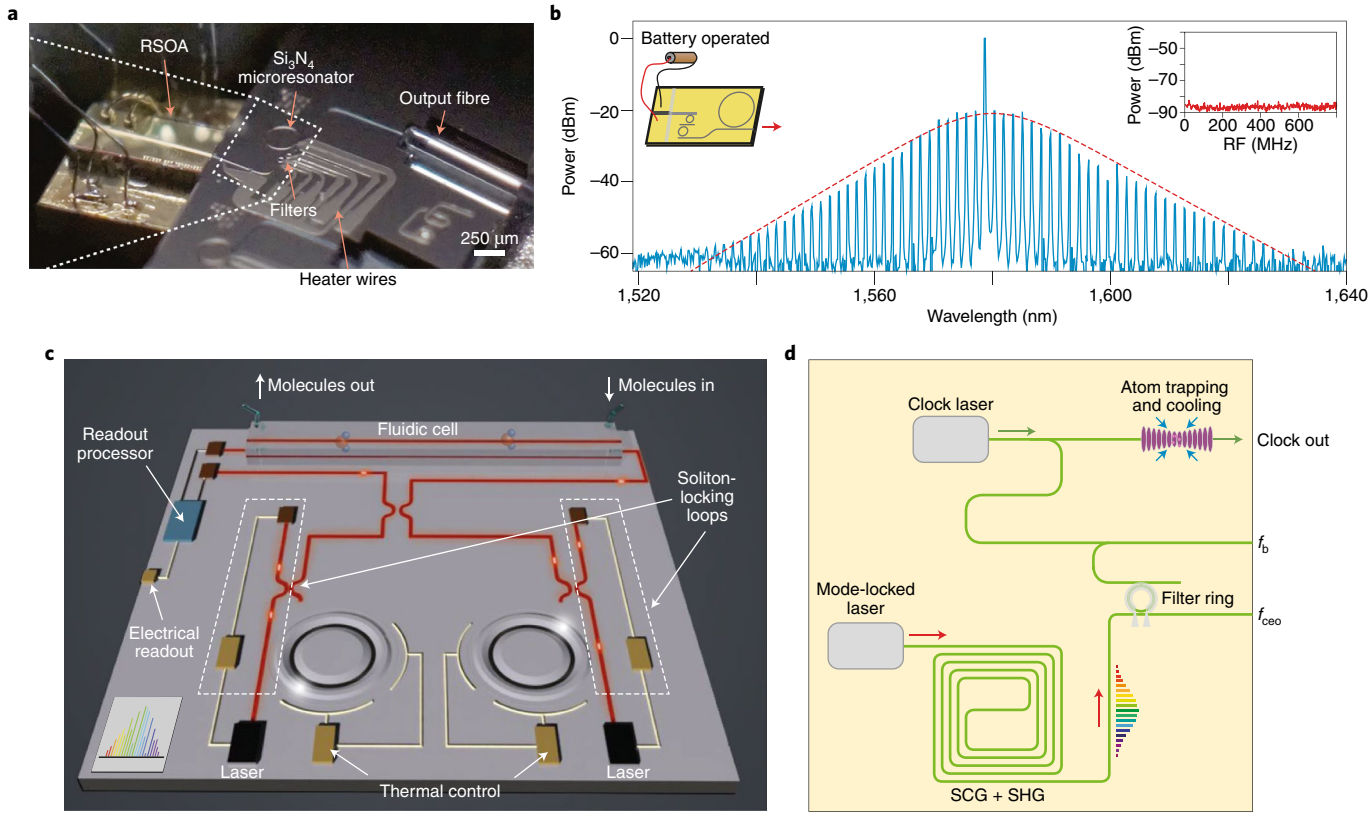

Fig. 6 | Integrated frequency comb source and potential implementations. a, Photograph of a fully integrated comb source. A reflecting semiconductor optical amplifier (RSOA) is edge-coupled to the Si_3N_4 chip and supplied with electric current via wirebonds, while the comb output is measured using an optical fibre. **b**, Generated comb while operating with an AAA battery[156]. The inset shows the RF spectrum representative of a low-noise mode-locked comb. **c**, Artist's conception of a dual-comb spectrometer based on a recent discrete dual-comb spectroscopy demonstration[120]. Spectroscopy of molecules suspended in a fluid is shown. Component colour coding: Si_3N_4 waveguides (red lines), dual parallel electrical traces for thermal control (shown as single gold lines), laser sources (black), detectors (brown), loop-control electronics (gold) and readout processing electronics (blue). The dual-comb spectrometer includes soliton-locking loops and thermal control for the resonators. Note that soliton pulses (white) appear in the resonators. **d**, Schematic of an integrated optical atomic clock based on SCG. An integrated mode-locked laser is used to pump a Si_3N_4 spiral waveguide for simultaneous second-harmonic generation (SHG) and SCG for *f*-2*f* interferometry and f_{CEO} detection. A section of the SCG output is filtered and mixed with the clock laser, which is stabilized to an atomic transition, for stabilization of the comb spacing. f_b is the beat frequency between the clock laser and the nearest comb line and f_{ceo} is the carrier–envelope offset frequency of the mode-locked laser. Figure adapted from: **a**,**b**, ref. [156], Springer Nature Limited; **c**, ref. [120], Springer Nature Limited.

effect may ultimately limit how small the comb spacing can be for mode-locked Kerr combs based on these platforms.

Material platforms. *Silicon nitride.* As with SCG in waveguides, silicon nitride has proven to be an exceptional platform for generating microresonator combs due to its relatively high index contrast and nonlinearity[109] and the highest quality (*Q*) factors (>10 million) (refs. [110–112]) demonstrated in a non-silica-based chip platform. Since the first observation[82], numerous key demonstrations of OFCs in this platform have been realized, including octave-spanning combs[113–115], very low threshold power for soliton generation[111,116], thermally controlled mode-locking[89], and the ability to produce combs out in the mid-infrared[117]. Key advances in fabrication include reducing surface roughness to the sub-ångström level via chemical–mechanical polishing to achieve $Q > 37$ million (ref. [111]) and the development of the photonic Damascene process that allows for large waveguide sizes and ultrasmooth preform reflow[112] to produce high *Q*. Arguably, this platform represents the one, to date, that has shown the greatest promise in realizing ultra-broadband devices that are fully integrated while potentially being CMOS-compatible.

Silica. Despite the low nonlinearity of silica glass, its extremely low loss allows for ultra-high microresonator *Q* (>875 million) (ref. [118]) that can produce strong nonlinear interactions and operation at low pump powers. Silica microwedge resonators have been developed that allow for significant dispersion control[119] and chip-compatible design via Si_3N_4–bus coupling while maintaining high *Q*, and, more recently, a fabrication process has been developed that allows for chip-based integration through use of a Si_3N_4–bus waveguide[120]. As a result of the very low loss and high transparency associated with silica, soliton combs have been generated with spacings in the gigahertz range[121] and down to the near-visible regime with the potential to go to even shorter wavelengths[122].

Silicon. Although silicon has relatively high loss compared with silica or silicon nitride, the relatively large nonlinearity allows for modest pump powers to produce broad combs, and its high transmission to wavelengths up to 8 μm make it ideally suited for KCG in the mid-infrared. For pump wavelengths below 2.2 μm, achieving parametric oscillation and comb generation is not possible due to two-photon absorption[123], but by suitable shortening of the free-carrier lifetime or operating above 3.2 μm, broadband combs[124] that

can be mode-locked are possible[125]. Both thermal and electrical injection can be used to tune and mode-lock the comb[74].

Other materials. Kerr-comb generation has been observed in a number of other chip-based platforms including diamond[126], aluminium nitride[127,128], aluminium gallium arsenide[129], gallium phosphide[130] and lithium niobate[131]. Of these platforms, only in aluminium nitride have DKSs been demonstrated[128]. Since a number of these materials exhibit an intrinsic $\chi^{(2)}$ nonlinearity, they offer the possibility of shifting the combs into the visible regime through second-harmonic and sum-frequency generation[130,132], allowing for f–$2f$ interferometry in a single element and rapid tuning of the properties of the generated comb via the electro-optic effect[133].

Applications. The promise of microresonator-based combs offers the potential for low-power operation in a fully integrated structure. A number of key demonstrations of microresonator-based combs for a wide variety of applications in spectroscopy, telecommunications, pulse shaping, frequency synthesis, distance ranging, astronomy and biological imaging have been realized.

Spectral measurements. A powerful approach to obtain optical spectra rapidly and with high precision is DCS[18]. Chip-based platforms offer an intrinsically straightforward approach to producing two microresonators that generate nearly identical combs due to the inherent precision of the photonic nanofabrication processes. Sources for DCS based on KCG have been achieved in the telecommunications band[92,134,135] and in the mid-infrared[136]. One promising implementation to further simplify DCS is to use a single microresonator and use counter-propagating pump waves to produce counter-rotating solitons[137,138] that can have slightly different round-trip times due to non-reciprocal nonlinear phase shifts for pump fields with different powers. Another approach is to simultaneously excite different spatial modes that have slightly different comb spacings[139]. It is possible to utilize scanning comb techniques to achieve higher resolution and resolve spectral features associated with gas-phase transitions using a dual-cavity scheme[140]. An important application in which the relatively large comb spacing of microresonator combs can be useful is for the calibration of telescope spectrometers for use in the search for exoplanets[141,142].

Telecommunications. For communications based on wavelength-division multiplexing, KCG offers the prospect of producing many single-frequency sources that all will be highly stabilized to a frequency grid via stabilization of only the single-frequency pump laser and the microresonator[82,143]. Soliton-mode-locked combs were used to realize very high data transmission rates (50 Tb s^{-1}) via wavelength-division multiplexing using a Si_3N_4 microresonator over 179 comb lines[144]. Normal-GVD combs also offer the potential as a wavelength-division multiplexing source for long-distance communication[98]. Additional functionalities for telecommunications that have been demonstrated with Si_3N_4 microresonators include multicasting[145] and reconfigurable optical tapped-delay-lines[146].

Distance ranging. A soliton-mode-locked dual-comb source can be used to perform high-precision distance ranging down to submicrometre resolution[147] and at very high speeds[148].

Timing and clocks. A particularly useful application for microresonator combs is their use in creating highly compact all-optical clocks that link the microwave and optical domains. While no octave-spanning combs with electronically detectable FSRs have been generated to date, there have been demonstrations of locking to Rb resonance lines[149] and 2–f to 3–f self-referencing using additional lasers[86]. Recent work has shown that it is possible to synchronize two soliton-mode-locked combs via weak photonic coupling separated by more than 20 m of fibre[93].

Frequency synthesis. The use of OFCs to provide a high-precision frequency 'ruler' allows for a frequency-stabilized laser to be locked to the comb and tuned to very high precision, realizing a source in which the absolute frequency can be specified to very high accuracy. Recent tour-de-force work[114] has shown that such frequency synthesis is possible using integrated components including two interlaced microresonator combs, one of which is octave-spanning with a 1-THz comb spacing and a second that has a much narrower bandwidth but has a 22-GHz FSR that can be easily detected electronically through direct detection.

Microwave generation and pulse synthesis. Chip-based Kerr combs offer the potential for creating highly compact and high-precision integrated RF and microwave devices[150]. A number of important functionalities based on chip-based microresonators include RF filters[151], a Hilbert transformer[152], intensity differentiator[153], optical true time delay[154] and wave shaping[155].

Future outlook

The initial promise of realizing chip-based comb devices that can be highly compact, portable and operate with low powers is coming to fruition[156–158], including the demonstration of an integrated comb generator that draws less than 100 mW of electrical power and can be operated with an AAA battery[156] (Fig. 6a,b). We expect rapid progress towards devices that fully integrate both photonics and control electronics on-chip. Realizing fully integrated mode-locked pump-lasers with waveguide SCG devices has proven to be challenging due to the difficulties in creating chip-based mode-locked lasers with subpicosecond laser pulses that are electrically pumped. However, recent work[159–161] indicates that such sources will be realized in the not-too-distant future and could allow for octave-spanning comb spectra with comb spacings that can be detected electronically. Overall, over the next decade, we foresee wide adoption of these chip-comb technologies across a broad range of environments, with applications in chemical sensing, LIDAR, telecommunications, photonic frequency synthesis, temporal metrology, astronomy, biological imaging, and microwave synthesis and generation.

Received: 20 November 2018; Accepted: 7 January 2019;
Published online: 21 February 2019

References

1. Cundiff, S. T. & Ye, J. Colloquium: femtosecond optical frequency combs. *Rev. Mod. Phys.* **75**, 325–342 (2003).
2. Ranka, J. K., Windeler, R. S. & Stentz, A. J. Visible continuum generation in air–silica microstructure optical fibers with anomalous dispersion at 800 nm. *Opt. Lett.* **25**, 25–27 (2000).
3. Del'Haye, P. et al. Optical frequency comb generation from a monolithic microresonator. *Nature* **450**, 1214–1217 (2007).
4. Dudley, J. M., Genty, G. & Coen, S. Supercontinuum generation in photonic crystal fiber. *Rev. Mod. Phys.* **78**, 1135–1184 (2006).
5. Savchenkov, A. A. et al. Low threshold optical oscillations in a whispering gallery mode CaF_2 resonator. *Phys. Rev. Lett.* **93**, 243905 (2004).
6. Kippenberg, T. J., Spillane, S. M. & Vahala, K. J. Kerr-nonlinearity optical parametric oscillation in an ultrahigh-Q toroid microcavity. *Phys. Rev. Lett.* **93**, 083904 (2004).
7. Grelu, P. (ed) *Nonlinear Optical Cavity Dynamics: From Microresonators to Fiber Lasers* (Wiley, Berlin, 2015).
8. Haus, H. A. Mode-locking of lasers. *IEEE J. Sel. Top. Quant. Electron.* **6**, 1173–1185 (2000).
9. Lugiato, L. A. & Lefever, R. Spatial dissipative structures in passive optical systems. *Phys. Rev. Lett.* **58**, 2209–2211 (1987).
10. Kippenberg, T. J., Gaeta, A. L., Lipson, M. & Gorodetsky, M. L. Dissipative Kerr solitons in optical microresonators. *Science* **361**, eaan8083 (2018).
11. Foster, M. A. et al. Broad-band optical parametric gain on a silicon photonic chip. *Nature* **441**, 960–963 (2006).
12. Lettieri, S., Di Finizio, S., Maddalena, P., Ballarini, V. & Giorgis, F. Second-harmonic generation in amorphous silicon nitride microcavities. *Appl. Phys. Lett.* **81**, 4706–4708 (2002).

13. Levy, J. S., Foster, M. A., Gaeta, A. L. & Lipson, M. Harmonic generation in silicon nitride ring resonators. *Opt. Express* **19**, 11415–11421 (2011).
14. Billat, A. et al. Large second harmonic generation enhancement in Si_3N_4 waveguides by all-optically induced quasi-phase-matching. *Nat. Commun.* **8**, 1016 (2017).
15. Akhmediev, N. & Karlsson, M. Cherenkov radiation emitted by solitons in optical fibers. *Phys. Rev. A* **51**, 2602–2607 (1995).
16. Brabec, T. & Krausz, F. Nonlinear optical pulse propagation in the single-cycle regime. *Phys. Rev. Lett.* **78**, 3283–3285 (1997).
17. Skryabin, D. V. & Gorbach, A. V. Colloquium: looking at a soliton through the prism of optical supercontinuum. *Rev. Mod. Phys.* **82**, 1287–1299 (2010).
18. Coddington, I., Newbury, N. & Swann, W. Dual-comb spectroscopy. *Optica* **3**, 414–426 (2016).
19. Hsieh, I.-W. et al. Supercontinuum generation in silicon photonic wires. *Opt. Express* **15**, 15242–15249 (2007).
20. Liang, T. K. & Tsang, H. K. Role of free carriers from two-photon absorption in Raman amplification in silicon-on-insulator waveguides. *Appl. Phys. Lett.* **84**, 2745–2747 (2004).
21. Kuyken, B. et al. Mid-infrared to telecom-band supercontinuum generation in highly nonlinear silicon-on-insulator wire waveguides. *Opt. Express* **19**, 20172–20181 (2011).
22. Lau, R. K. W. et al. Octave-spanning mid-infrared supercontinuum generation in silicon nanowaveguides. *Opt. Lett.* **39**, 4518–4521 (2014).
23. Kuyken, B. et al. An octave-spanning mid-infrared frequency comb generated in a silicon nanophotonic wire waveguide. *Nat. Commun.* **6**, 6310 (2015).
24. Singh, N. et al. Mid-infrared supercontinuum generation from 2 to 6 μm in a silicon nanowire. *Optica* **2**, 797–802 (2015).
25. Kou, R. et al. Mid-IR broadband supercontinuum generation from a suspended silicon waveguide. *Opt. Lett.* **43**, 1387–1390 (2018).
26. Safioui, J. et al. Supercontinuum generation in hydrogenated amorphous silicon waveguides at telecommunication wavelengths. *Opt. Express* **22**, 3089–3097 (2014).
27. Shen, L. et al. Four-wave mixing and octave-spanning supercontinuum generation in a small core hydrogenated amorphous silicon fiber pumped in the mid-infrared. *Opt. Lett.* **39**, 5721–5724 (2014).
28. Dave, U. D. et al. Telecom to mid-infrared spanning supercontinuum generation in hydrogenated amorphous silicon waveguides using a Thulium doped fiber laser pump source. *Opt. Express* **21**, 32032–32039 (2013).
29. Leo, F., Safioui, J., Kuyken, B., Roelkens, G. & Gorza, S.-P. Generation of coherent supercontinuum in a-Si:H waveguides: experiment and modeling based on measured dispersion profile. *Opt. Express* **22**, 28997–29007 (2014).
30. Halir, R. et al. Ultrabroadband supercontinuum generation in a CMOS-compatible platform. *Opt. Lett.* **37**, 1685–1687 (2012).
31. Epping, J. P. et al. On-chip visible-to-infrared supercontinuum generation with more than 495 THz spectral bandwidth. *Opt. Express* **23**, 19596–19604 (2015).
32. Zhao, H. et al. Visible-to-near-infrared octave spanning supercontinuum generation in a silicon nitride waveguide. *Opt. Lett.* **40**, 2177–2180 (2015).
33. Wang, T. et al. Supercontinuum generation in bandgap engineered, back-end CMOS compatible silicon rich nitride waveguides. *Laser Photon. Rev.* **9**, 498–506 (2015).
34. Liu, X. et al. Octave-spanning supercontinuum generation in a silicon-rich nitride waveguide. *Opt. Lett.* **41**, 2719–2722 (2016).
35. Johnson, A. R. et al. Octave-spanning coherent supercontinuum generation in a silicon nitride waveguide. *Opt. Lett.* **40**, 5117–5120 (2015).
36. Mayer, A. S. et al. Frequency comb offset detection using supercontinuum generation in silicon nitride waveguides. *Opt. Express* **23**, 15440–15451 (2015).
37. Klenner, A. et al. Gigahertz frequency comb offset stabilization based on supercontinuum generation in silicon nitride waveguides. *Opt. Express* **24**, 11043–11053 (2016).
38. Okawachi, Y. et al. Coherent, directional supercontinuum generation. *Opt. Lett.* **42**, 4466–4469 (2017).
39. Guo, H. et al. Mid-infrared frequency comb via coherent dispersive wave generation in silicon nitride nanophotonic waveguides. *Nat. Photon.* **12**, 330–335 (2018).
40. Carlson, D. R. et al. Photonic-chip supercontinuum with tailored spectra for counting optical frequencies. *Phys. Rev. Appl.* **8**, 014027 (2017).
41. Carlson, D. R. et al. Self-referenced frequency combs using high-efficiency silicon-nitride waveguides. *Opt. Lett.* **42**, 2314–2317 (2017).
42. Okawachi, Y. et al. Carrier envelope offset detection via simultaneous supercontinuum and second harmonic generation in a silicon-nitride waveguide. *Opt. Lett.* **43**, 4627–4630 (2018).
43. Billat, A. et al. Large second harmonic generation enhancement in Si_3N_4 waveguides by all-optically induced quasi-phase-matching. *Nat. Commun.* **8**, 1016 (2017).
44. Gai, X., Madden, S., Choi, D.-Y., Bulla, D. & Luther-Davies, B. Dispersion engineered $Ge_{11.5}As_{24}Se_{64.5}$ nanowires with a nonlinear parameter of 136 $W^{-1}m^{-1}$ at 1550 nm. *Opt. Express* **18**, 18866–18874 (2010).
45. Karim, M. R., Rahman, B. M. A. & Agrawal, G. P. Mid-infrared supercontinuum generation using dispersion-engineered $Ge_{11.5}As_{24}Se_{64.5}$ chalcogenide channel waveguide. *Opt. Express* **23**, 6903–6914 (2015).
46. Herzog, A. et al. Chalcogenide waveguides on a sapphire substrate for mid-IR applications. *Opt. Lett.* **39**, 2522–2525 (2014).
47. Yu, Y. et al. Experimental demonstration of linearly polarized 2–10 μm supercontinuum generation in a chalcogenide rib waveguide. *Opt. Lett.* **41**, 958–961 (2016).
48. Lamont, M. R. E., Luther-Davies, B., Choi, D.-Y., Madden, S. & Eggleton, B. J. Supercontinuum generation in dispersion engineered highly nonlinear ($\gamma = 10$ /W/m) As_2S_3 chalcogenide planar waveguide. *Opt. Express* **16**, 14938–14944 (2008).
49. Tremblay, J.-E., Malinowski, M., Richardson, K. A., Fathpour, S. & Wu, M. C. Picojoule-level octave-spanning supercontinuum generation in chalcogenide waveguides. *Opt. Express* **26**, 21358–21363 (2018).
50. Hammani, K. et al. Octave spanning supercontinuum in titanium dioxide waveguides. *Appl. Sci.* **8**, 543 (2018).
51. Dave, U. D. et al. Dispersive-wave-based octave-spanning supercontinuum generation in InGaP membrane waveguides on a silicon substrate. *Opt. Lett.* **40**, 3584–3587 (2015).
52. Ettabib, M. A. et al. Broadband telecom to mid-infrared supercontinuum generation in a dispersion-engineered silicon germanium waveguide. *Opt. Lett.* **40**, 4118–4121 (2015).
53. Sinobad, M. et al. Mid-infrared octave spanning supercontinuum generation to 8.5 μm in silicon-germanium waveguides. *Optica* **5**, 360–366 (2018).
54. Yuan, J. et al. Mid-infrared octave-spanning supercontinuum and frequency comb generation in a suspended germanium-membrane ridge waveguide. *J. Lightwave Technol.* **35**, 2994–3002 (2017).
55. Hickstein, D. D. et al. Ultrabroadband supercontinuum generation and frequency-comb stabilization using on-chip waveguides with both cubic and quadratic nonlinearities. *Phys. Rev. Appl.* **8**, 014025 (2017).
56. Phillips, C. R. et al. Supercontinuum generation in quasi-phase-matched $LiNbO_3$ waveguide pumped by a Tm-doped fiber laser system. *Opt. Lett.* **36**, 3912–3914 (2011).
57. Oh, D. Y. Supercontinuum generation in an on-chip silica waveguide. *Opt. Lett.* **39**, 1046–1048 (2014).
58. Oh, D. Y. et al. Coherent ultra-violet to near-infrared generation in silica ridge waveguides. *Nat. Commun.* **8**, 13922 (2016).
59. Picqué, N. & Hänsch, T. W. Frequency comb spectroscopy. *Nat. Photon.* https://doi.org/10.1038/s41566-018-0347-5 (2019).
60. Hu, J. et al. Fabrication and testing of planar chalcogenide waveguide integrated microfluidic sensor. *Opt. Express* **15**, 2307–2314 (2007).
61. Hu, H. et al. Single-source chip-based frequency comb enabling extreme parallel data transmission. *Nat. Photon.* **12**, 469–473 (2018).
62. Herr, T. et al. Temporal solitons in optical microresonators. *Nat. Photon.* **8**, 145–152 (2014).
63. Kippenberg, T. J., Holzwarth, R. & Diddams, S. A. Microresonator-based optical frequency combs. *Science* **332**, 555–559 (2011).
64. Pasquazi, A. et al. Micro-combs: a novel generation of optical sources. *Phys. Rep.* **729**, 1–81 (2018).
65. Cole, D. C., Lamb, E. S., Del'Haye, P., Diddams, S. A. & Papp, S. B. Soliton crystals in Kerr resonators. *Nat. Photon.* **11**, 671–676 (2017).
66. Bao, C. et al. Observation of Fermi-Pasta-Ulam recurrence induced by breather solitons in an optical microresonator. *Phys. Rev. Lett.* **117**, 163901 (2016).
67. Yu, M. Breather soliton dynamics in microresonators. *Nat Commun.* **8**, 14569 (2017).
68. Lucas, E., Karpov, M., Guo, H., Gorodetsky, M. L. & Kippenberg, T. J. Breathing dissipative solitons in optical microresonators. *Nat Commun.* **8**, 736 (2017).
69. Lugiato, L. A. & Lefever, R. Spatial dissipative structures in passive optical systems. *Phys. Rev. Lett.* **58**, 2209–2211 (1987).
70. Matsko, A. B. et al. Mode-locked Kerr frequency combs. *Opt. Lett.* **36**, 2845–2847 (2011).
71. Chembo, Y. K. & Menyuk, C. R. Spatiotemporal Lugiato-Lefever formalism for Kerr-comb generation in whispering-gallery-mode resonators. *Phys. Rev. A* **87**, 053852 (2013).
72. Coen, S., Randle, H. G., Sylvestre, T. & Erkintalo, M. Modeling of octave-spanning Kerr frequency combs using a generalized mean-field Lugiato-Lefever model. *Opt. Lett.* **38**, 37–39 (2013).
73. Lamont, M. R. E., Okawachi, Y. & Gaeta, A. L. Route to stabilized ultrabroadband microresonator-based frequency combs. *Opt. Lett.* **38**, 3478–3481 (2013).
74. Yu, M., Okawachi, Y., Griffith, A. G., Lipson, M. & Gaeta, A. L. Mode-locked mid-infrared frequency combs in a silicon microresonator. *Optica* **3**, 854–860 (2016).
75. Herr, T. et al. Universal formation dynamics and noise of Kerr-frequency combs in microresonators. *Nat. Photon.* **6**, 480–487 (2012).

76. Skryabin, D. V. & Kartashov, Y. V. Self-locking of the frequency comb repetition rate in microring resonators with higher order dispersions. *Opt. Express* **25**, 27442–27451 (2017).
77. Coen, S. & Erkintalo, M. Universal scaling laws of Kerr frequency combs. *Opt. Lett.* **38**, 1790–1792 (2013).
78. Okawachi, Y. et al. Bandwidth shaping of microresonator-based frequency combs via dispersion engineering. *Opt. Lett.* **39**, 3535–3538 (2014).
79. Bao, C. et al. High-order dispersion in Kerr comb oscillators. *J. Opt. Soc. Am. B* **34**, 715–725 (2017).
80. Savchenkov, A. A. et al. Tunable optical frequency comb with a crystalline whispering gallery mode resonator. *Phys. Rev. Lett.* **101**, 093902 (2008).
81. Grudinin, I. S., Yu, N. & Maleki, L. Generation of optical frequency combs with a CaF_2 resonator. *Opt. Lett.* **34**, 878–880 (2009).
82. Levy, J. S. et al. CMOS-compatible multiple wavelength oscillator for on-chip optical interconnects. *Nat. Photon.* **4**, 37–40 (2010).
83. Razzari, L. et al. CMOS-compatible integrated optical hyper-parametric oscillator. *Nat. Photon.* **4**, 41–45 (2010).
84. Saha, K. et al. Modelocking and femtosecond pulse generation in chip-based frequency combs. *Opt. Express* **21**, 1335–1343 (2013).
85. Foster, M. A. et al. Silicon-based monolithic optical frequency comb source. *Opt. Express* **19**, 14233–14239 (2011).
86. Brasch, V. et al. Photonic chip-based optical frequency comb using soliton Cherenkov radiation. *Science* **351**, 357–360 (2016).
87. Guo, H. et al. Universal dynamics and deterministic switching of dissipative Kerr solitons in optical microresonators. *Nat. Phys.* **13**, 94–102 (2017).
88. Yi, X., Yang, Q.-F., Yang, K. Y. & Vahala, K. Imaging soliton dynamics in optical microcavities. *Nat. Commun.* **9**, 3565 (2018).
89. Joshi, C. et al. Thermally controlled comb generation and soliton modelocking in microresonators. *Opt. Lett.* **41**, 2565–2568 (2016).
90. Brasch, V., Geiselmann, M., Pfeiffer, M. H. P. & Kippenberg, T. J. Bringing short-lived dissipative Kerr soliton states in microresonators into a steady state. *Opt. Express* **24**, 29312–29320 (2016).
91. Cole, D. C. et al. Kerr-microresonator solitons from a chirped background. *Optica* **5**, 1304–1310 (2018).
92. Dutt, A. et al. On-chip dual comb source for spectroscopy. *Sci. Adv.* **4**, e1701858 (2018).
93. Jang, J. K. et al. Synchronization of coupled optical microresonators. *Nat. Photon.* **12**, 688–693 (2018).
94. Liang, W. et al. Generation of a coherent near-infrared Kerr frequency comb in a monolithic microresonator with normal GVD. *Opt. Lett.* **39**, 2920–2923 (2014).
95. Xue, X. et al. Mode-locked dark pulse Kerr combs in normal-dispersion microresonators. *Nat. Photon.* **9**, 594–600 (2015).
96. Xue, X. et al. Normal-dispersion microcombs enabled by controllable mode interactions. *Laser Photon. Rev.* **9**, L23–L28 (2015).
97. Parra-Rivas, P., Gomila, D., Knobloch, E., Coen, S. & Gelens, L. Origin and stability of dark pulse Kerr combs in normal dispersion resonators. *Opt. Lett.* **41**, 2402–2405 (2016).
98. Fülöp, A. et al. Long-haul coherent communications using microresonator-based frequency combs. *Opt. Express* **25**, 26678–26688 (2017).
99. Jang, J. K. et al. Dynamics of mode-coupling-induced microresonator frequency combs in normal dispersion. *Opt. Express* **24**, 28794–28803 (2016).
100. Herr, T. et al. Mode spectrum and temporal soliton formation in optical microresonators. *Phys. Rev. Lett.* **113**, 123901 (2014).
101. Ramelow, S. et al. Strong polarization mode coupling in microresonators. *Opt. Lett.* **39**, 5134–5137 (2014).
102. Chembo, Y. K., Grudinin, I. S. & Yu, N. Spatiotemporal dynamics of Kerr-Raman optical frequency combs. *Phys. Rev. A* **92**, 043818 (2015).
103. Milián, C., Gorbach, A. V., Taki, M., Yulin, A. V. & Skryabin, D. V. Solitons and frequency combs in silica microring resonators: interplay of the Raman and higher-order dispersion effects. *Phys. Rev. A* **92**, 033851 (2015).
104. Karpov, M. et al. Raman self-frequency shift of dissipative Kerr solitons in an optical microresonator. *Phys. Rev. Lett.* **116**, 103902 (2016).
105. Yi, X., Yang, Q.-F., Yang, K. Y. & Vahala, K. Theory and measurement of the soliton self-frequency shift and efficiency in optical microcavities. *Opt. Lett.* **41**, 3419–3422 (2016).
106. Wang, Y., Anderson, M., Coen, S., Murdoch, S. G. & Erkintalo, M. Stimulated Raman scattering imposes fundamental limits to the duration and bandwidth of temporal cavity solitons. *Phys. Rev. Lett.* **120**, 053902 (2018).
107. Yang, Q.-F., Yi, X., Yang, K. Y. & Vahala, K. Stokes solitons in optical microcavities. *Nat. Phys.* **13**, 53–57 (2017).
108. Okawachi, Y. et al. Competition between Raman and Kerr effects in microresonator comb generation. *Opt. Lett.* **42**, 2786–2789 (2017).
109. Moss, D. J., Morandotti, R., Gaeta, A. L. & Lipson, M. New CMOS-compatible platforms based on silicon nitride and Hydex for nonlinear optics. *Nat. Photon.* **7**, 597–607 (2013).
110. Xuan, Y. et al. High-*Q* silicon nitride microresonators exhibiting low-power frequency comb initiation. *Optica* **3**, 1171–1180 (2016).
111. Ji, X. et al. Ultra-low-loss on-chip resonators with sub-milliwatt parametric oscillation threshold. *Optica* **4**, 619–624 (2017).
112. Pfeiffer, M. H. P. et al. Ultra-smooth silicon nitride waveguides based on the Damascene reflow process: fabrication and loss origins. *Optica* **5**, 884–892 (2018).
113. Okawachi, Y. et al. Octave-spanning frequency comb generation in a silicon nitride chip. *Opt. Lett.* **36**, 3398–3400 (2011).
114. Spencer, D. T. et al. An optical-frequency synthesizer using integrated photonics. *Nature* **557**, 81–85 (2018).
115. Pfeiffer, M. H. P. et al. Octave-spanning dissipative Kerr soliton frequency combs in Si_3N_4 microresonators. *Optica* **4**, 684–691 (2017).
116. Liu, J. et al. Ultralow-power chip-based soliton microcombs for photonic integration. *Optica* **5**, 1347–1353 (2018).
117. Luke, K., Okawachi, Y., Lamont, M., Gaeta, A. & Lipson, M. Broadband mid-infrared frequency comb generation in a Si_3N_4 microresonator. *Opt. Lett.* **40**, 4823–4826 (2015).
118. Lee, H. et al. Chemically etched ultrahigh-*Q* wedge-resonator on a silicon chip. *Nat. Photon.* **6**, 369–373 (2012).
119. Yang, K. Y. et al. Broadband dispersion-engineered microresonator on a chip. *Nat. Photon.* **10**, 316–320 (2016).
120. Yang, K. Y. et al. Bridging ultrahigh-*Q* devices and photonic circuits. *Nat. Photon.* **12**, 297–302 (2018).
121. Suh, M.-G. & Vahala, K. Gigahertz-repetition-rate soliton microcombs. *Optica* **5**, 65–66 (2018).
122. Lee, S. H. et al. Towards visible soliton microcomb generation. *Nat. Commun.* **8**, 1295 (2017).
123. Lau, R. K. W., Lamont, M. R. E., Okawachi, Y. & Gaeta, A. L. Effects of multiphoton absorption on parametric comb generation in silicon microresonators. *Opt. Lett.* **40**, 2778–2781 (2015).
124. Griffith, A. G. et al. Silicon-chip mid-infrared frequency comb generation. *Nat. Commun.* **6**, 6299 (2015).
125. Hansson, T., Modotto, D. & Wabnitz, S. Mid-infrared soliton and Raman frequency comb generation in silicon microrings. *Opt. Lett.* **39**, 6747–6750 (2014).
126. Hausmann, B. J. M., Bulu, I., Venkataraman, V., Deotare, P. & Lončar, M. Diamond nonlinear photonics. *Nat. Photon.* **8**, 369–374 (2014).
127. Jung, H., Stoll, R., Guo, X., Fischer, D. & Tang, H. X. Green, red, and IR frequency comb line generation from single IR pump in AlN microring resonator. *Optica* **1**, 396–399 (2014).
128. Gong, Z. et al. High-fidelity cavity soliton generation in crystalline AlN micro-ring resonators. *Opt. Lett.* **43**, 4366–4369 (2018).
129. Pu, M., Ottaviano, L., Semenova, E. & Yvind, K. Efficient frequency comb generation in AlGaAs-on-insulator. *Optica* **3**, 823–826 (2016).
130. Wilson, D. J. et al. Integrated gallium phosphide nonlinear photonics. Preprint at https://arxiv.org/abs/1808.03554 (2018).
131. Wang, C. et al. On-chip Kerr frequency comb generation in lithium niobate microresonators. In *Conf. Lasers Electro-Optics, OSA Technical Digest (online)* Paper SW4M.3 (OSA, 2018).
132. Guo, X. et al. Efficient generation of a near-visible frequency comb via Cherenkov-like radiation from a Kerr microcomb. *Phys. Rev. Appl.* **10**, 014012 (2018).
133. Jung, H., Fong, K. Y., Xiong, C. & Tang, H. X. Electrical tuning and switching of an optical frequency comb generated in aluminum nitride microring resonators. *Opt. Lett.* **39**, 84–87 (2014).
134. Suh, M.-G., Yang, Q.-F., Yang, K. Y., Yi, X. & Vahala, K. J. Microresonator soliton dual-comb spectroscopy. *Science* **354**, 600–603 (2016).
135. Pavlov, N. G. et al. Soliton dual frequency combs in crystalline microresonators. *Opt. Lett.* **42**, 514–517 (2017).
136. Yu, M. et al. Silicon-chip-based mid-infrared dual-comb spectroscopy. *Nat. Commun.* **9**, 1869 (2018).
137. Yang, Q.-F., Yi, X., Yang, K. Y. & Vahala, K. Counter-propagating solitons in microresonators. *Nat. Photon.* **11**, 560–564 (2017).
138. Joshi, C. et al. Counter-rotating cavity solitons in a silicon nitride microresonator. *Opt. Lett.* **43**, 547–550 (2018).
139. Lucas, E. et al. Spatial multiplexing of soliton microcombs. *Nat. Photon.* **12**, 699–705 (2018).
140. Yu, M. et al. Gas-phase microresonator-based comb spectroscopy without an external pump laser. *ACS Photon.* **5**, 2780–2785 (2018).
141. Obrzud, E. et al. A microphotonic astrocomb. *Nat. Photon.* **13**, 31–35 (2019).
142. Suh, M.-G. et al. Searching for exoplanets using a microresonator astrocomb. *Nat. Photon.* **13**, 25–30 (2019).
143. Levy, J. S. et al. High-performance silicon-nitride-based multiple-wavelength source. *Photon. Technol. Lett.* **24**, 1375–1377 (2012).
144. Marin-Palomo, P. et al. Microresonator-based solitons for massively parallel coherent optical communications. *Nature* **546**, 274–279 (2017).
145. Bao, C. et al. Demonstration of optical multicasting using Kerr frequency comb lines. *Opt. Lett.* **41**, 3876–3879 (2016).

146. Willner, A. N. et al. Scalable and reconfigurable optical tapped-delay-line for multichannel equalization and correlation using nonlinear wave mixing and a Kerr frequency comb. *Opt. Lett.* **43**, 5563–5566 (2018).
147. Trocha, P. et al. Ultrafast optical ranging using microresonator soliton frequency combs. *Science* **359**, 887–891 (2018).
148. Suh, M.-G. & Vahala, K. J. Soliton microcomb range measurement. *Science* **359**, 884–887 (2018).
149. Papp, S. B. et al. Microresonator frequency comb optical clock. *Optica* **1**, 10–14 (2014).
150. Wu, J. Y. et al. RF photonics: an optical microcombs' perspective.*IEEE J. Sel. Top. Quantum Electron.* **24**, 6101020 (2018).
151. Xue, X. et al. Programmable single-bandpass photonic RF filter based on Kerr comb from a microring. *J. Light. Technol.* **32**, 3557–3565 (2014).
152. Nguyen, T. G. et al. Integrated frequency comb source based Hilbert transformer for wideband microwave photonic phase analysis. *Opt. Express* **23**, 22087–22097 (2015).
153. Xu, X. et al. Reconfigurable broadband microwave photonic intensity differentiator based on an integrated optical frequency comb source. *APL Photon.* **2**, 096104 (2017).
154. Xu, X. et al. Advanced RF and microwave functions based on an integrated optical frequency comb source. *Opt. Express* **26**, 2569–2583 (2018).
155. Ferdous, F. et al. Spectral line-by-line pulse shaping of on-chip microresonator frequency combs. *Nat. Photon.* **5**, 770–776 (2011).
156. Stern, B., Ji, X., Okawachi, Y., Gaeta, A. L. & Lipson, M. Battery-operated integrated frequency comb generator. *Nature* **562**, 401–405 (2018).
157. Volet, N. et al. Micro-resonator soliton generated directly with a diode laser. *Laser Photon. Rev.* **12**, 1700307 (2018).
158. Raja, A. S. et al. Electrically pumped photonic integrated soliton microcomb. *Nat. Commun.* https://doi.org/10.1038/s41467-019-08498-2 (2019).
159. Uvin, S. et al. Narrow line width frequency comb source based on an injection-locked III-V-on-silicon mode-locked laser. *Opt. Express* **24**, 5277–5286 (2016).
160. Guzmán, R., Gordon, C., Orbe, L. & Carpintero, G. 1-GHz InP on-chip monolithic extended cavity colliding-pulse mode-locked laser. *Opt. Lett.* **42**, 2318–2321 (2017).
161. Liu, S. et al. 490 fs pulse generation from passively mode-locked single section quantum dot laser directly grown on on-axis GaP/Si. *Electron. Lett.* **54**, 432–433 (2018).

Acknowledgements

We are grateful to Y. Okawachi and M. Yu for help in preparing Table 1 and Figs. 1, 2 and 6. This work was supported by AFOSR program award number FA9550-15-1-0303 and the ARPA-E PINE program.

Author contributions

All authors discussed and edited the content in the manuscript.

Competing interests

The authors declare no competing interests.

Additional information

Reprints and permissions information is available at www.nature.com/reprints.

Correspondence should be addressed to A.L.G.

Publisher's note: Springer Nature remains neutral with regard to jurisdictional claims in published maps and institutional affiliations.

© Springer Nature Limited 2019